

Which Milky Way masses are consistent with the slightly declining 5-25 kpc rotation curve?

Y. Jiao¹, F. Hammer¹, J. L. Wang², and Y. B. Yang¹

¹ GEPI, Observatoire de Paris, Université PSL, CNRS, Place Jules Janssen 92195, Meudon, France, e-mail: francois.hammer@obspm.fr

² CAS Key Laboratory of Optical Astronomy, National Astronomical Observatories, Beijing 100101, China

Received 00 MM 0000 / Accepted 00 MM 0000

ABSTRACT

Context. Discoveries of extended rotation curves have suggested the presence of dark matter in spiral galaxy haloes. It has led to many studies that estimated the galaxy total mass, mostly by using the Navarro Frenk and White (NFW) density profile.

Aims. We aim at verifying how the choice of the dark-matter profile may affect the predicted values of extrapolated total masses.

Methods. We have considered the recent Milky Way rotation curve, firstly because of its unprecedented accuracy, and secondly because the Galactic disk is amongst the least affected by past major mergers having fully reshaped the initial disk.

Results. We find that the use of NFW profile (or its generalized form, gNFW) for calculating the dark-matter contribution to the Milky Way rotation curve generates apparently inconsistent results, e.g., an increase of the baryonic mass leads to increase of the dark matter mass. Furthermore we find that NFW and gNFW profile narrow the total mass range, leading to a possible methodological bias particularly against small MW masses. By using the Einasto profile that is more appropriate to represent cold dark matter haloes, we finally find that the Milky Way slightly decreasing rotation curve favors total mass that can be as small as $2.6 \times 10^{11} M_{\odot}$, disregarding any other dynamical tracers further out in the Milky Way. It is inconsistent with values larger than $18 \times 10^{11} M_{\odot}$ for any kind of CDM dark-matter halo profiles, under the assumption that stars and gas do not influence the predicted dark matter distribution in the Milky Way.

Conclusions. This methodological paper encourages the use of the Einasto profile for characterizing rotation curves with the aim of evaluating their total masses.

Key words. Galaxy: kinematics and dynamics – Galaxy: structure – dark matter – methods: numerical

1. Introduction

Gaia DR2 provided accurate stellar proper motions for calculating the circular velocity curve of the Milky Way (MW) up to 25 kpc (Eilers et al. 2019; Mróz et al. 2019). The result has been based on a thorough analysis of a very large sample of 26,000 RGB stars in the MW disk (Eilers et al. 2019) resulting into a slightly but robustly determined decline of the circular velocity from 5 to 25 kpc. While Eilers et al. (2019, see also Hogg et al. 2019) have used spectrophotometric distances in their analysis, their finding is confirmed by Mróz et al. (2019) using 773 Classical Cepheids with precise distances. Subsequent analyses of these rotation curves (RCs) have lead to MW total mass near or well below $10^{12} M_{\odot}$ (Eilers et al. 2019; de Salas et al. 2019; Grand et al. 2019; Karukes et al. 2020). The latter study has used a considerable number of baryonic matter distribution to derive the overall mass distribution, while the second one has accounted for very large error bars after cumulating all the systematics described in details by Eilers et al. (2019).

The accuracy of the MW RC also allows to test different mass profiles for the dark matter (DM) distribution in the MW halo. Recent studies have shown that the three parameter Einasto profile (Einasto 1965, see also Retana-Montenegro et al. 2012) provides a better description of the CDM halo density profile than NFW (Navarro et al. 2004, 2010; Gao et al. 2008), and

even than the three parameter generalized, gNFW (Klypin et al. 2016).

In this paper, we propose to test both Einasto and NFW (Navarro et al. 1997) density profiles and their impact to the total mass estimates when fitting spiral rotation curves. Here we consider the MW RC because of its unprecedented accuracy, and also because the MW past history is likely quiescent when compared to other spirals (Hammer et al. 2007), since the last MW major merger occurred ~ 10 Gyr ago, as it has been recently confirmed from the resulting debris identified by Gaia DR1 (Belokurov et al. 2018) and soon confirmed by Gaia DR2 (Haywood et al. 2018; Helmi et al. 2018).

In Section 2 we present our proposed treatment of the error bars for the Eilers et al. (2019) RC, and then the choice and mathematical descriptions of both baryon and DM models. In Section 3 we compare the χ^2 probability distribution for DM represented by either NFW or Einasto profiles. In Section 4 we discuss which mass range is consistent with the combined constraints provided by the fit of the MW RC, and by adopting DM halo profiles from the Cold Dark Matter (CDM) theory.

2. Methods

2.1. Rotation curve and error bars

Eilers et al. (2019) provided a thorough analysis of the possible systematic errors that may affect the MW RC and summarized

(see their Figure 4) four different kinds of systematics. The first kind includes the neglected term in their Jeans equation (see their Equation 3) that is a cross-term made by the vertical density gradient of the product of the radial and vertical velocities. This term is found to be small but not negligible at large distances. For example, Mackereth et al. (2019) showed that vertical velocities are larger for young stars, which is expected since the gaseous disk is likely affected by (former) gas infall. This may influence the derived RC because Eilers et al. (2019) selected relatively young stars (< 4 Gyrs) for the MW RC, in order to avoid asymmetric drift effects.

However the effect is expected to be small (< 5 km/s at 12 kpc) when compared to the RC amplitude. The second kind is empirical and it is an estimate of error variations with radius after splitting the sample into two parts. We consider here only the first kind of systematics because it likely includes the second one.

Adding to this, Eilers et al. (2019) considered a third category of systematics, which nature is quite different, because it proportionally applies in a same way to all RC points. It is revealed by the three almost horizontal lines in the Figure 4 of Eilers et al. (2019). This last category of systematics includes the effect of changing the Sun distance to the Galactic Center (blue dash line), the proper motion of the latter (grey line), and it can be extended to the change in scalelength (yellow dash line). These uncertainties have to be applied to the derived mass as a whole after the fitting analysis. Added together, they correspond to an additional systematic uncertainty of $\sim 2\%$ on velocity scale and $\sim 4\%$ on mass scale. We notice in agreement with Christina Eilers (Eilers, 2020, private communication) that summing up all the errors of Eilers et al. (2019) Figure 4 (as it has been done by de Salas et al. 2019) would strongly overestimate the error bars (see the above discussion), which leads to a dilution of the significance of the MW RC.

In the following we adopt the same parameters for the Sun position and velocity than Eilers et al. (2019). Karukes et al. (2020) have shown that the choice of the Sun velocity may significantly affect the determination of its mass, while it has been considered determined at a 2-3% level by Eilers et al. (2019).

2.2. Milky Way baryonic mass models

The contribution of the baryonic components to the MW mass or RC is still uncertain and this may well affect the determination of the DM distribution. Following Karukes et al. (2020) we adopt here a large number of models from the literature to describe the MW baryonic component, as it is described below. There are still debates about the baryonic component and its distribution into bulge, disk, thick disk, gas and even halo gas (see the review by Bland-Hawthorn & Gerhard 2016), and some modeling are also introducing a ionized gas-component (Cautun et al. 2020). The basic idea is to cope with uncertainties on baryons by using a very large grid of possible models, though we are aware that some baryons models may be not fully consistent with other important constraints from vertical dynamics of the disk stars (Bovy & Rix 2013) or from micro-lensing (Wegg et al. 2016).

Pouliasis et al. (2017) generated a new axisymmetric model (Model I) including a spherical bulge, a thin and a thick disk. This model satisfies a number of observational constraints: stellar densities at the solar vicinity, thin and thick disk scale lengths and heights, and the absolute value of the perpendicular force K_z as a function of distance to the Galactic centre. Although the disk is made of a thin and a thick disk, the associated density profiles are both described by Miyamoto-Nagai profile (Eq. 1). Pouliasis

Table 1. Parameters for Model I, Model A&S and Model S

Parameter	Model I	Model A&S	Model S
$M_{\text{bulge}}(10^{10} M_{\odot})$	1.067	1.406	2.5
$M_{\text{thin}}(10^{10} M_{\odot})$	3.944	8.561	11.2
$M_{\text{thick}}(10^{10} M_{\odot})$	3.944	—	—
$a_{\text{thin}}(\text{kpc})$	5.3	5.3178	5.73
$a_{\text{thick}}(\text{kpc})$	2.6	—	—
$b_{\text{bulge}}(\text{kpc})$	0.3	0.3873	0.87
$b_{\text{thin}}(\text{kpc})$	0.25	0.25	—
$b_{\text{thick}}(\text{kpc})$	0.8	—	—

et al. (2017) concludes that Model I supersedes the axisymmetric model (Model A&S) proposed by Allen & Santillan (1991), because there is growing evidences for an important thick disk component and because the bulge is less prominent and less classical than assumed in Model A&S. The Model A&S consists of a stellar thin disk of Miyamoto-Nagai profile (Miyamoto & Nagai 1975) and a central bulge of Plummer profile (Binney & Tremaine 2011). The description of the bulge and disks for both Model I and Model A&S are expressed in the form (Pouliasis et al. 2017) for (R, z) cylindrical coordinates:

$$\rho_{\text{thin}}(R, z) = \frac{b_{\text{thin}}^2 M_{\text{thin}}}{4\pi} \times \frac{\left(R^2 a_{\text{thin}} + 3(z^2 + b_{\text{thin}}^2)^{1/2}\right) \left(a_{\text{thin}} + (z^2 + b_{\text{thin}}^2)^{1/2}\right)^2}{\left(R^2 + \left[a_{\text{thin}} + (z^2 + b_{\text{thin}}^2)^{1/2}\right]^2\right)^{5/2} (z^2 + b_{\text{thin}}^2)^{3/2}} \quad (1)$$

$$\rho_{\text{bulge}}(r) = \frac{3b_{\text{bulge}}^2 M_{\text{bulge}}}{4\pi (r^2 + b_{\text{bulge}}^2)^{5/2}} \quad (2)$$

where $r = \sqrt{R^2 + z^2}$, and M_{thin} , M_{thick} , M_{bulge} , a_{thin} , a_{thick} , b_{thin} , b_{thick} , b_{bulge} are the disks and bulge mass and scale constants, respectively (see Table 1).

Sofue (2015) presented a model (Model S) of the MW by attempting to fit a ‘grand rotation curve’¹. The bulge was approximated by de Vaucouleurs profile (de Vaucouleurs 1958). We chose to adopt a Plummer profile (Eq. (2)) for the bulge, and the disk is assumed to follow an exponential thin density profile. The surface mass density of the disk is expressed as (Sofue 2015):

$$\Sigma_d(R) = \Sigma_0 \exp(-R/a_{\text{thin}}) \quad (3)$$

where Σ_0 is the central value and a_{thin} is the scale radius (see Table 1). This model provides the largest baryonic mass when compared to other models in the literature (see Figure 1). Nevertheless we consider it as useful for testing the impact of an extremely large baryonic mass for the MW disk and bulge.

A great addition to our choices of baryonic components was presented by Iocco et al. (2015), and they allow several possible combinations of models for the bulge and the disk. For the

¹ Sofue (2015) called ‘grand rotation curve’ the combination of the actual rotation curves (up to 20-25 kpc) with estimates based on orbital motions of objects beyond 25 kpc in the MW halo, e.g., distant globular clusters.

Table 2. Parameters for bulge E2 and bulge G2

Parameter	bulge E2	bulge G2
$M_{\text{bulge}}(10^{10} M_{\odot})$	2.41	2.12
$x_b(\text{kpc})$	0.899	1.239
$y_b(\text{kpc})$	0.386	0.609
$z_b(\text{kpc})$	0.250	0.438

Table 3. Parameters of disk CM J and dJ

Parameter	disk CM	disk J	disk dJ
$M_{\text{thin}}(10^{10} M_{\odot})$	3.11	3.17	3.33
$M_{\text{thick}}(10^{10} M_{\odot})$	0.82	0.90	0.78
$L_1(\text{kpc})$	2.75	2.6	2.6
$L_2(\text{kpc})$	4.1	3.6	4.1
$H_1(\text{kpc})$	0.25	0.3	0.25
$H_2(\text{kpc})$	0.75	0.9	0.75

bulge we choose two triaxial mass density distributions E2 and G2 presented by Stanek et al. (1997) :

$$\text{E2} : \rho_{\text{bulge}}(x, y, z) = \rho_0 e^{-r_1} \quad (4)$$

$$\text{G2} : \rho_{\text{bulge}}(x, y, z) = \rho_0 e^{-r_2^2/2} \quad (5)$$

with :

$$r_1^2 = \frac{x^2}{x_b^2} + \frac{y^2}{y_b^2} + \frac{z^2}{z_b^2}, r_2^2 = \left(\frac{x^2}{x_b^2} + \frac{y^2}{y_b^2} \right)^2 + \frac{z^4}{z_b^4} \quad (6)$$

where (x, y, z) are the coordinates along the major, intermediate and minor axes. For the thin and thick disks we adopt double exponential of the three models (CM from Calchi Novati & Mancini 2011, dJ from de Jong et al. 2010 and J from Jurić et al. 2008) as it is described below (see Table 3):

$$\text{CM} : \rho(R, z) = \Sigma_{\text{thin}} \left(\frac{1}{2H_1} \exp \left(-\frac{R}{L_1} - \frac{z}{H_1} \right) + f_{\text{thick}} \frac{1}{2H_2} \exp \left(-\frac{R}{L_2} - \frac{z}{H_2} \right) \right) \quad (7)$$

$$\text{J, dJ} : \rho(R, z) = \rho_{\text{thin}, \odot} \left(e^{R_0/L_1} \exp \left(-\frac{R}{L_1} - \frac{z}{H_1} \right) + f_{\text{thick}} e^{R_0/L_2} \exp \left(-\frac{R}{L_2} - \frac{z}{H_2} \right) \right) \quad (8)$$

From decreasing order of baryonic mass, Model S, Model A&S, and then Model I are assuming significantly higher mass baryonic components than the 6 combinations of bulge (G2, E2) and disk (CM, dJ, J), which is illustrated by Figure 1 or by comparing Table 1 with Tables 2 and 3.

2.3. Milky Way dark matter models

Here we consider the NFW and Einasto profiles for describing the density profiles of DM halos in spherical coordinates (r). The generalized NFW profile (gNFW, see Zhao 1996) can be expressed as in de Salas et al. (2019):

$$\rho(r) = \frac{\rho_0}{(r/r_0)^\gamma (1 + r/r_0)^{3-\gamma}} \quad (9)$$

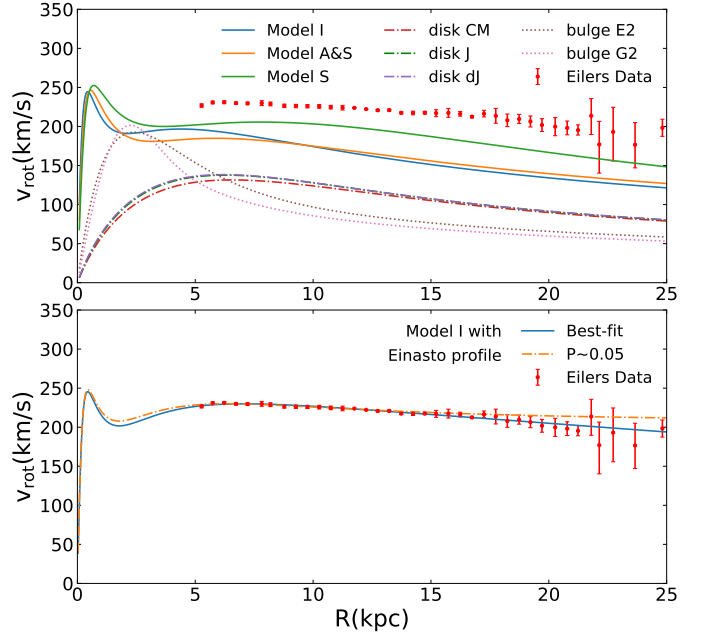


Fig. 1. *Top:* Contribution to the rotation curve of different baryonic models and model components. Red points indicate the rotation curve of the Milky Way from Eilers et al. (2019). The error-bars are estimated via bootstrapping and include the systematic uncertainties from the neglected term (see text). *Bottom:* Fit of the rotation curve by the best-fit model (solid blue curve, total mass of $2.8 \cdot 10^{11} M_{\odot}$), and with the most massive MW model for which the χ^2 probability reaches $P=0.05$ (orange dash-dotted line, total mass of $18 \cdot 10^{11} M_{\odot}$), both associated to the baryonic distribution from model I of Pouliasis et al. (2017).

where r_0 is the scale radius, ρ_0 is the characteristic dark matter density. For $\gamma=1$ the profile becomes the NFW profile (Navarro et al. 1997) for which we investigate which parameters are able to fit the MW RC, after letting free the two NFW parameters, r_0 and $m_{\text{NFW}} = 4 \pi \rho_0 r_0^3$, from 2 to 100 kpc, and from 1 to $50 \cdot 10^{11} M_{\odot}$, respectively. For the gNFW profile we let the additional parameter, γ , to vary from 0.1 to 3 (see also Karukes et al. 2020). For each tested mass configurations, we verified later that the investigated parameter space is sufficiently large to avoid having missed any solution.

Using the Retana-Montenegro et al. (2012) mathematical framework, the Einasto profile can be written as:

$$\rho(r) = \rho_0 \exp \left[-\left(\frac{r}{h} \right)^{1/n} \right] \quad (10)$$

where n can determine how fast the density decreases with r . To investigate which models are able to fit the MW RC, we let free the three Einasto parameters, $b_E = 3 \times n$, $h_{\text{red}} = h^{1/n}$, and $m_E = 4 \pi \rho_0 h^3 n \Gamma(b_E)$, from 3 to 30, 0.05 to 3, and from 1 to $50 \cdot 10^{11} M_{\odot}$, respectively. For each tested mass configuration, we verified later that the investigated parameter space is sufficiently large to avoid any missing solution.

In order to determine a non-indefinite total MW mass, the DM halo mass has to be limited by the virial radius, R_{vir} , which enclosed M_{vir} , which is the virial mass. We define the virial radius is the radius of the sphere for which the average dark matter density equals 200 times the critical density of the Universe ρ_{cr} . In this work we adopt a critical density of $\rho_{\text{cr}} = 1.34 \times 10^{-7} M_{\odot}/\text{pc}^3$ which comes from Hinshaw et al. (2013). With this definition, the relation between virial radius and virial

mass is :

$$M_{\text{vir}} = 200 \times \frac{4\pi}{3} \rho_{\text{cr}} R_{\text{vir}}^3 \quad (11)$$

3. Results

3.1. MW total mass derivation and χ^2 probability

The MW total potential can be obtained through the Poisson equation:

$$\nabla^2 \Phi_{\text{tot}} = 4\pi G \sum_i \rho_i \quad (12)$$

after adding all the different MW mass components. The theoretical estimate of the circular velocity is derived at different disk radii (R) from the potential Φ_{tot} of the Galaxy, through:

$$v_c^2(R) = R \frac{\partial \Phi_{\text{tot}}}{\partial R} \Big|_{z \approx 0} \quad (13)$$

We apply the χ^2 method to fit the RC and calculate its associated probability, for which we have tested an extremely large parameter space. The χ^2 is calculated by the sum at each disk radius R_i :

$$\chi^2 = \sum_i^N \frac{(v_{\text{mod},i} - v_{\text{obs},i})^2}{\sigma_i^2} \quad (14)$$

where v_{mod} is the modeled circular velocity for the cumulative baryons + DM profiles, v_{obs} is the observed circular velocity and σ_{stat} is the statistical uncertainty of the measurement so that $\sigma_{\text{stat},i} = (\sigma_{v_{\text{obs},i}}^+ + \sigma_{v_{\text{obs},i}}^-)/2$ to which we have added the systematic uncertainty $\sigma_{\text{sys},i}$ to calculate σ_i (see Sect. 2.1 and Table in Appendix A). Hence the χ^2 probability can be expressed as :

$$\text{Prob}\left(\frac{\chi^2}{2}, \frac{N - \nu}{2}\right) = \frac{\gamma\left(\frac{N - \nu}{2}, \frac{\chi^2}{2}\right)}{\Gamma\left(\frac{N - \nu}{2}\right)} \quad (15)$$

where N is the number of independent observed velocity points in the Eilers et al. (2019) RC and ν is the number of degrees of freedom.

To fit the MW RC we have investigated a very large parameter space, allowing for, e.g., MW total mass from 1 to $50 \times 10^{11} M_{\odot}$. In Figure 2 each point ($P(\chi^2)$, M_{tot}) represents an investigated baryon+DM model. The top panels of Figure 2 present the χ^2 probability for Model I baryon profile (Pouliasis et al. 2017) when associated to either Einasto (left), NFW (middle), and gNFW (right) profiles. The first profile shows that high χ^2 probabilities are reached for small MW masses. On the contrary, there is no similar trend for the NFW profile, which selects a narrow range of MW masses to fit the RC. The situation is improved with gNFW, though it does not recover the whole range of masses, especially missing total masses below $5 \times 10^{11} M_{\odot}$. The bottom panels present the same for the model S, for which probabilities are very low when associated either to Einasto or to NFW DM profiles. Examination of the RC fit shows that the baryonic mass is so large that its radial profile is setting-up most of the expected RC (see also Figure 1), leading to differences with the observed RC at almost every radii. This is not unexpected since the model S is clearly at odds for the MW, with its disk plus bulge mass being larger than that of M31, while half this value is more likely (see, e.g., Hammer et al. 2007).

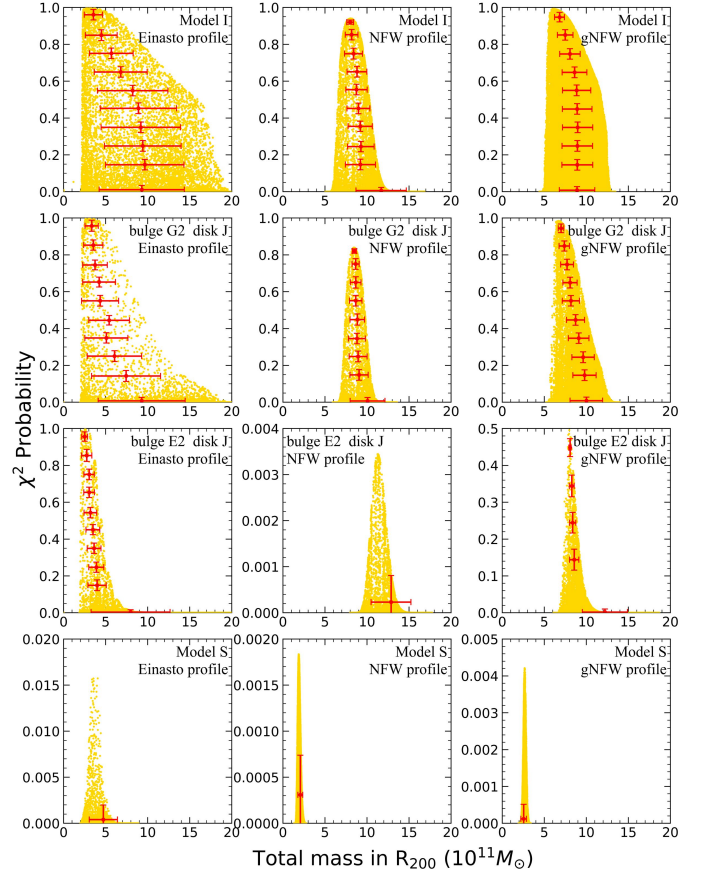


Fig. 2. χ^2 probability associated to the combination of different baryonic models with Einasto, NFW, or gNFW mass profiles for the DM. From the top to the bottom rows, it shows Model I, bulge G2+disk J, bulge E2+disk J, and model S, respectively. The red points and error-bars are the average and 1σ uncertainties.

The two middle row panels of Figure 2 compares the results when changing bulge G2 (top) to E2 (bottom), both added to the disk J. The former provides a similar behavior than Model I associated either to Einasto or to NFW DM profiles. In using Einasto profile for DM, we found that by increasing the bulge mass by 15% (from G2 to E2) is sufficient to exclude large MW total mass values. This is not unexpected since by increasing the baryonic mass one may expect a smaller amount of DM mass to reproduce the MW RC. Moreover, a too large bulge may limit the number of possible solutions able to fit the RC at low radii. However, for the NFW profile we find that a bulge mass increase from G2 to E2 is sufficient to prevent an efficient reproduction of the MW RC, providing very low χ^2 values. We also find that the associated total (and DM) masses are larger than that for the G2 bulge, which comes at odd with our expectations. We notice that the two above properties disappear when using the 3-parameter gNFW model, which could be due to the fact that for $\gamma < 1$, this profile is less cuspy, and then less affected by bulge mass changes.

The above motivates us to investigate further why adding an additional baryonic mass could lead to an increase of the DM mass when the later is modeled by the NFW density profile. We have tested how changing the amount of baryonic mass may affect the NFW DM mass. We have considered a range of baryonic

mass scaled on that of Model I, with scale factors f varying from 0.85 to 1.15. For $f=0.85, 1$, and 1.15 , it confirms that by increasing the baryonic mass, the NFW DM model leads to a significant increase of the DM mass from $5.9, 7.2$, and $10.7 \times 10^{11} M_{\odot}$, respectively. This is an unexpected behavior since the DM role is to compensate the lack of baryonic mass for fitting a given RC. Our first explanation was to relate it to the two-parameter nature of the NFW profile. However, a similar (though less pronounced) behavior affects the gNFW profile. For $f=0.85, 1$, and 1.15 , the gNFW DM model also leads to an increase of the DM mass from $4.8, 5.25$, and $7.1 \times 10^{11} M_{\odot}$, respectively. It suggests the following mechanism: for an increasing baryonic mass, the NFW DM scale radius (r_0 , see Eq. 9) has to increase for diluting the DM mass from 5 to 25 kpc (the latest point of the RC). Because the NFW and gNFW outer density slope is almost constant and shallow (-3) at large radii, this automatically leads to increasing DM masses. This points out to a possible methodological problem when using NFW (or gNFW) for fitting the RC as well as for estimating the mass of a galaxy from it.

3.2. Systematics due to NFW and gNFW when estimating total mass

To evaluate the differences between Einasto and NFW DM density profiles in fitting the MW RC, we need to ensure that our method does not depend on the initial conditions. In particular the parameter grid could influence our results, since we realize in looking at Figure 2 that the three-parameter space (Einasto or gNFW) could be more difficult to be populated than the two-parameter space (NFW). We further perform for each model combination several Monte Carlo simulations accounting also for the variance due to the RC error bars assumed to follow a Gaussian distribution, in order to fill as much as possible the high probability space in the $(P(\chi^2), M_{\text{tot}})$ plane.

Solid lines in Figure 3 identify the envelop for each baryonic + DM model, which is defined as being the largest χ^2 probability calculated in mass slices with sizes of $0.3 \times 10^{11} M_{\odot}$. We assume that only χ^2 probabilities larger than 0.05 correspond to a ‘good fit’ of the RC, which we verified after examination of the latter. For comparison, Figure 3 also shows the averaged probabilities.

Figure 3 shows that for all baryonic models, using NFW or gNFW profile for the DM leads to a narrower range of total masses for the MW than when using Einasto profile. Conversely, using the Einasto profile suffices to sample most the points generated by the NFW profile in the $(P(\chi^2), M_{\text{tot}})$ plane. We find that the total mass solutions based on the NFW and gNFW profiles are often included into those from the Einasto profile, while using NFW does not match with the largest χ^2 probabilities found by the Einasto model (compare the peaks of the magenta and green solid lines). However, in the case of a massive bulge (E2, especially when associated to disk J), the three-parameter gNFW may sample total MW mass values that cannot be reached by Einasto.

Table 4 gives the estimated total masses based on the minimal χ^2 values (‘best fit’, highest probabilities) or on averaging the χ^2 probabilities in each mass slices (‘average’). As in Figure 3 rows are sorted from heavy to light baryonic models. It indicates that best fit of the MW RC for all baryonic models, but A&S, are unavoidably related to small total masses (from 2.3 to $3.3 \times 10^{11} M_{\odot}$) if a Einasto profile is chosen for the DM. Conversely to that, adopting NFW (or gNFW) profile for the DM leads to much larger total mass values by factor 2 to 4.

Within our studied models, Model A&S possesses the second largest baryonic mass, close to $10^{11} M_{\odot}$, and we have inves-

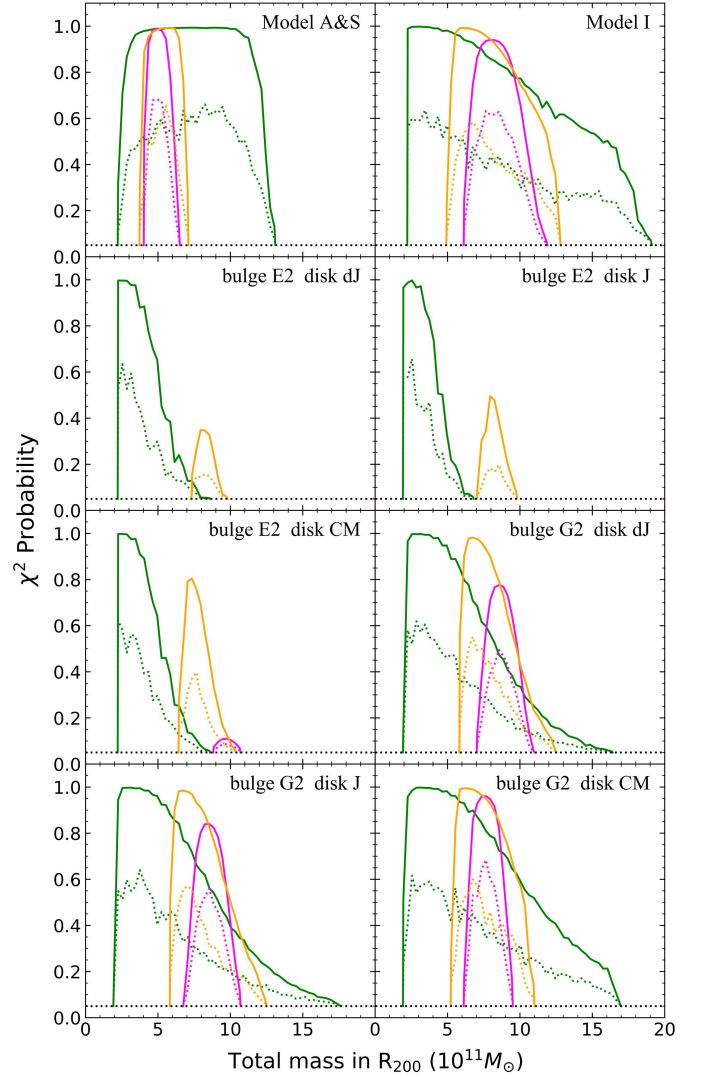


Fig. 3. Maximal (solid lines) and averaged (dotted lines) χ^2 probabilities for the different baryonic models studied in the paper. Model names are labelled in each panels, with Einasto, NFW, and gNFW mass predictions in green, magenta, and orange, respectively. The two panels associated to baryonic model E2+dJ and E2+J show no histogram for NFW because this density profile fails to reproduce the MW RC. The horizontal dotted lines indicates the χ^2 probability limit of 0.05 below which a model is found to be not compelling for fitting the MW RC.

tigated why it provides such different behavior than other baryonic models, especially Model I. Besides baryonic masses that differ by 11%, the main difference between the two models is the presence of a thick disk incorporating half the disk mass in Model I, with a scalelength that is half that of the thin disk of both Models I and A&S. By modifying Model I thick disk scalelength to a larger value, we find that this suffices to provide a similar behavior than Model A&S for the normalized cumulative probabilities of both NFW and Einasto DM profiles. As previously noticed for model S, this suggests that an extended and relatively massive baryonic disk is setting-up a significant part of the RC shape.

Considering ‘averaged’ total masses slightly improves the similarities between predictions from NFW and Einasto DM mass profiles. This is true for Models A&S and I, which lead to almost consistent NFW and Einasto values of total masses. However, for lighter baryonic models, NFW profile for DM still

leads to mass larger by factors from 1.5 to 3 when compared to that resulting from the Einasto profile. The NFW (and at a lower extent the gNFW) profile appears to preferentially select a narrow range of total masses, excluding in particular the small mass values that are favored when using the Einasto profile.

4. Discussion

4.1. Limitations of this study and comparison with other works

This paper goal is mostly methodological, i.e., searching for the range of total MW masses that reproduce the MW RC, and then evaluating which mass density profile seem to be the more appropriate for estimating the DM mass. We focus on the sole rotation curve provided by Gaia DR2 (Eilers et al. 2019; Mróz et al. 2019) because its accuracy is several times better than any former studies (see Fig. 3 of Eilers et al. 2019). This is also because disk stars correspond to dynamical points well anchored into the stellar disk, which is supposed to be well in equilibrium with the MW potential. In this context, our study broadens the recent work made by de Salas et al. (2019) and by Karukes et al. (2020), because here we consider a wider range of baryonic matter models of the MW to fit the Gaia DR2 RC². Our resulting total masses for the baryonic Model I are indeed quite similar to the values in the de Salas et al. (2019) Table II, thus confirming that using Einasto profile will predict significantly smaller total MW masses than when using NFW or gNFW profiles. Small differences between the two works are probably due to the different schemes in interpreting the systematics of the Eilers et al. (2019) RC. We also retrieve similar results by Karukes et al. (2020) who also studied the impact of changing the DM density profile. While it goes in the same direction (Einasto profile predicts smaller total masses than gNFW), their results have not been applied on the accurate Gaia DR2 MW RC, which prevents a detailed comparison.

We are aware that using RC up to 25 kpc to constrain the mass density profile of the MW is a limited exercise since one needs to extrapolate to larger radii (see Figure 4). Extrapolations of total mass from a rotation curve is acknowledgedly non-correct, though it has been very often used in the literature either for giant spirals like the MW (see, e.g., Eilers et al. 2019 and references therein) or for dwarfs (see, e.g., Read et al. 2016). Other works are using different mass tracers such as globular clusters (Vasiliev 2019), massive and very bright stars (Deason et al. 2021), or dSph galaxies assumed to be satellites of the MW (Callingham et al. 2019). These methods have the advantage to sample objects much further in the MW halo, though their virial equilibrium with the MW potential is less guaranteed than for rotating disk stars (Eilers et al. 2019). The presence of a warp and flare occurring at radii larger than 12 kpc may also limit our study especially in the outer disk. However, the impact is possibly limited for our χ^2 fitting, since it is in the outer disk that error bars are very large because they account for the action of the vertical component (see Section 2.1 and Mackereth et al. 2019).

There are two other limitations of our study, the first one being linked to the adoption of a spherical halo, though constraints on the dark matter halo shape in the Milky Way are still weak (see Read 2014). The second one is linked to our choice of initial (flat) priors for DM halo profiles, and this could alter the validity of our results. We have compared our initial halos with

² Note that Karukes et al. (2020)'s study is not principally based on the Gaia DR2 RC, except in their Sect. 5.1, in which they favored a similarly low MW mass than in our work (see also their Fig. 8).

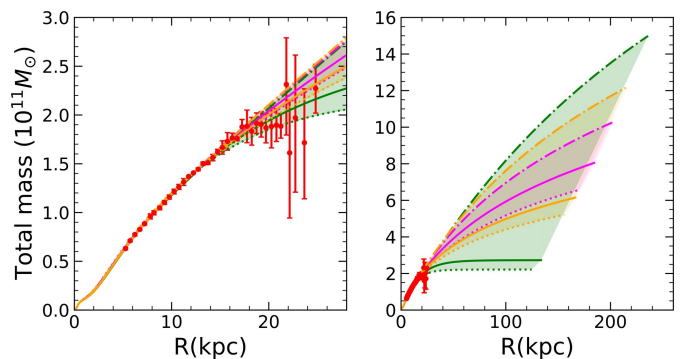


Fig. 4. Mass model derived from the MW RC (left panel) and extrapolated to larger radii (right panel), using Model I for the MW baryonic mass. The best fit, small and large mass model are shown in solid, dotted and dash-dotted lines from Einasto (green), NFW (magenta) and gNFW (orange), respectively. Areas showing the possible mass ranges are shaded using the same color code, indicating how NFW and gNFW are biasing the mass determination from RCs.

the Dutton & Macciò (2014)'s CDM simulations, in particular through the relation between concentration and total mass (M200). Our very broad range of parameters encompass all the Dutton & Macciò (2014, see Figure 3 of Udrescu et al. 2019) values in the range of $10^{11} - 10^{12.5} M_{\odot}$ and in the (c, M200) plane. The solutions that fit the MW rotation curve are also well within the range of simulated halos by Dutton & Macciò (2014).

Interestingly, our mass boundaries for χ^2 fitting of the MW RC encompass all the above derived values using other mass tracers. This let open the question of which mass density profile is the most appropriate to evaluate properly the DM contribution to the MW RC. During the submission of this paper, another study made by Cautun et al. (2020) has been published, providing a detailed analysis of the impact of baryons to the DM profile, resulting into a contracted halo in the spatial region where the RC is determined. While the total mass is assumed to be consistent within error bars with the Callingham et al. (2019) value ($M_{\text{tot}} = 1.17 \pm 0.18 \times 10^{12} M_{\odot}$), Cautun et al. (2020) succeeded to fit the MW RC that provided most of the constraints, given its accuracy. Together with our study, this leads us to three important remarks:

- By using only the MW RC as a constraint, we find that the Einasto mass density profile leads to the largest range of MW total masses able to reproduce its RC, while both NFW and gNFW profiles lead to narrow the mass range, in particular by excluding total mass ($M_{200} = M_{\text{tot}}$) values smaller than $\sim 5 \times 10^{11} M_{\odot}$;
- The contracted halo density profile could be difficult to be reproduced by NFW or by gNFW profiles (Cautun et al. 2020), while it is part of the solutions of this paper using an Einasto profile combined with the baryonic model of Cautun et al. (2020) (see Figure 5);
- We find that both NFW and gNFW profiles provide total masses that increase with baryonic masses (see rows four to nine in Table 4), which contradicts expectations that the DM presence is for compensating a lack of mass from baryons in a galaxy. This contrasts with Einasto predictions for which the DM mass is larger when the assumed baryonic mass is smaller.

It could have been envisioned that the above limitations of the NFW profile are related to its two-parameter nature, but this

Table 4. Models and associated baryonic mass (first and second columns), and estimated total mass using χ^2 probabilities for Einasto, NFW, and gNFW DM density profiles (third to eighth columns, all masses are given in units of $10^{11} M_\odot$). The total mass and mass ranges are evaluated by using the minimal χ^2 (best fit, columns 3 and 5) and by weighting total masses by their χ^2 probabilities (average, columns 4 and 6), altogether with associated 1σ uncertainties. The later also account for systematics related to the Galactic distance and its motion, as well as to change of the scalelength ($\sim 4\%$ on masses, see Sect. 2.1), which have been added to the quoted error bars in this Table.

Baryon model	M_{bar}	M_{tot} Einasto best fit	R_{200} Einasto best fit	M_{tot} Einasto average	M_{tot} NFW best fit	R_{200} NFW best fit	M_{tot} NFW average	M_{tot} gNFW best fit	R_{200} gNFW best fit	M_{tot} gNFW average
S	1.370	—	—	—	—	—	—	—	—	—
A&S	0.997	$7.36^{+3.11}_{-2.85}$	$186.22^{+20.07}_{-40.21}$	$7.20^{+2.24}_{-2.34}$	$4.93^{+1.03}_{-0.54}$	$151, 17^{+14.04}_{-12.30}$	$5.13^{+0.66}_{-0.60}$	$5.83^{+0.95}_{-0.66}$	$161.92^{+15.02}_{-12.13}$	$5.26^{+0.74}_{-0.66}$
I	0.896	$2.77^{+6.13}_{-0.29}$	$134.48^{+70.29}_{-9.12}$	$6.56^{+4.70}_{-3.12}$	$8.02^{+2.49}_{-0.97}$	$184.26^{+24.45}_{-13.59}$	$8.66^{+1.48}_{-1.45}$	$6.15^{+3.09}_{-0.76}$	$166.44^{+30.60}_{-13.34}$	$8.23^{+1.82}_{-1.61}$
E2 dJ	0.652	$2.37^{+1.03}_{-0.23}$	$127.63^{+17.75}_{-10.13}$	$3.01^{+0.70}_{-0.46}$	—	—	—	$7.93^{+0.85}_{-0.70}$	$186.47^{+8.52}_{-13.45}$	$8.42^{+0.68}_{-0.65}$
E2 J	0.648	$2.56^{+1.60}_{-0.13}$	$130.99^{+17.78}_{-14.46}$	$3.13^{+0.93}_{-0.82}$	—	—	—	$7.97^{+1.09}_{-0.74}$	$186.79^{+9.92}_{-14.62}$	$8.51^{+0.79}_{-0.75}$
E2 CM	0.634	$2.41^{+1.30}_{-0.75}$	$128.34^{+18.66}_{-18.43}$	$3.59^{+1.01}_{-0.81}$	$9.68^{+1.45}_{-0.51}$	$200.24^{+9.77}_{-14.37}$	$9.72^{+0.80}_{-0.89}$	$7.44^{+1.48}_{-0.61}$	$182.41^{+15.54}_{-11.74}$	$8.08^{+0.94}_{-0.93}$
G2 dJ	0.623	$3.08^{+3.72}_{-0.10}$	$139.3^{+48.34}_{-7.93}$	$4.10^{+2.40}_{-1.40}$	$8.58^{+1.30}_{-1.11}$	$192.00^{+10.12}_{-18.24}$	$9.01^{+1.06}_{-1.07}$	$6.82^{+2.20}_{-0.86}$	$176.89^{+20.79}_{-14.63}$	$8.26^{+1.47}_{-1.23}$
G2 J	0.619	$3.11^{+4.68}_{-0.14}$	$139.82^{+58.41}_{-6.41}$	$4.46^{+3.04}_{-1.61}$	$8.41^{+1.25}_{-1.30}$	$190.64^{+12.75}_{-16.62}$	$8.76^{+0.93}_{-1.09}$	$6.70^{+2.79}_{-0.74}$	$175.79^{+26.47}_{-13.41}$	$8.57^{+1.62}_{-1.53}$
G2 CM	0.605	$3.29^{+4.80}_{-0.28}$	$142.39^{+59.48}_{-10.11}$	$5.69^{+3.95}_{-2.49}$	$7.53^{+1.18}_{-0.93}$	$183.45^{+12.61}_{-14.05}$	$7.82^{+0.82}_{-0.89}$	$6.19^{+2.32}_{-0.58}$	$170.99^{+23.49}_{-11.31}$	$7.60^{+1.36}_{-1.19}$

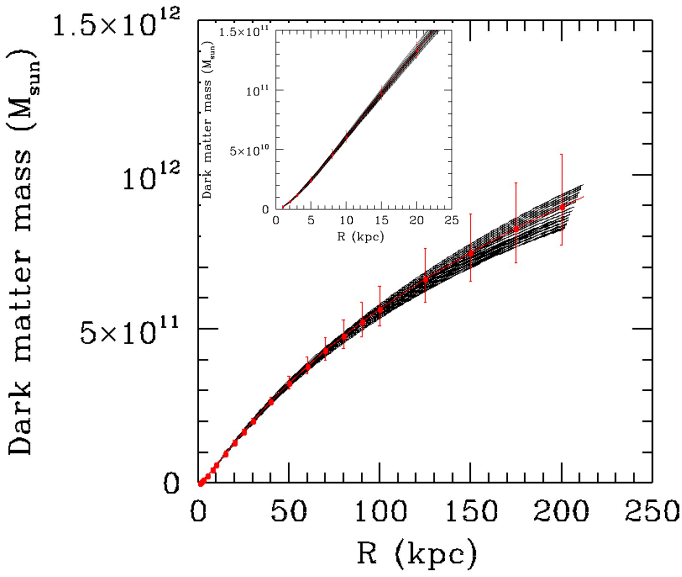


Fig. 5. Dark-matter enclosed mass versus radius for the mass profile of the contracted halo of Cautun et al. 2020, from which points and error bars are given in red colors. After assuming the same baryon content, the black curves show the result from 24 Einasto models that fit both the RC and the contracted halo. Total mass are very similar within few percent, and the only small difference is that R_{200} are ranging from 200 to 213 kpc instead of 218 kpc for the contracted halo of Cautun et al. 2020. The inset shows a zoom of the mass distribution below 25 kpc to show the similarity between the Einasto DM and the contracted halo near the range of radii of the RC.

seems to be ruled out by the (almost) similar behavior of the 3-parameter gNFW profile. Alternatively, this could be attributed to their density profile at outskirts. Both have an analytical form that imposes a constant slope of the density profile reaching -3 at large distances, leading to an enclosed mass value that is not converging since it increases as the logarithm of the radius. Investigations by Nesti & Salucci (2013) of the internal, $r < 5$ kpc MW kinematics showed that cuspy-like NFW (or gNFW for $\gamma > 0$) profile may also experience some difficulties when combined to baryonic mass.

4.2. Can the MW has a total mass as low as $2.6 \times 10^{11} M_\odot$?

Einasto profile fit of the RC points towards small total mass values for the MW (see Table 4, Figure 2 and Figure 3), disregarding any other dynamical tracers further out in the Milky Way. However, the main result of this paper is provided by the combination of RC fitting with either Einasto or NFW profile for the MW DM halo, leading to a MW total mass range between 2.5 to $18 \times 10^{11} M_\odot$ (see Figures 1-4). This range is consistent with many studies, including that based on other mass indicators, though they are generally discrepant with our lowest mass range. Figure 6 compares the orbital energy of globular clusters (GCs) from Vasiliev (2019) with that expected from the most likely (total mass: $2.6 \times 10^{11} M_\odot$) and the heaviest (total mass: $15 \times 10^{11} M_\odot$) MW mass model that could reproduce the MW RC when combining Model I for baryons and Einasto profile for DM. Both are consistent with having GCs gravitationally bounded to the MW, but one, Pyxis, which appears to be significantly discrepant for the lighter model. However, Pyxis eccentric orbit, metallicity, and age point to an extragalactic origin of Pyxis (Fritz et al. 2017). This indicates that in absence of other precise mass indicators from 25 to 70 kpc, it may be premature to conclude on the MW total-mass value from $2.6 \times 10^{11} M_\odot$ and $R_{200} = 135$ kpc (χ^2 probability = 0.999) to $15 \times 10^{11} M_\odot$ and $R_{200} = 236$ kpc (χ^2 probability = 0.35), and even $18 \times 10^{11} M_\odot$ with a χ^2 probability = 0.05.

We remark that a low value for the MW mass would have considerable consequences on, e.g., the orbits of many dSph galaxies. For example, Boylan-Kolchin et al. (2013) convincingly showed that a MW mass significantly larger than $10^{12} M_\odot$ is necessary to bound Leo I. Using the Boylan-Kolchin et al. (2013) phase space plot, Hammer et al. (2020) shows that Gaia DR2 orbits could indicate a passage more recent than 4 Gyr ago for many dSphs, assuming a total mass of $8.66 \times 10^{11} M_\odot$ for the MW (Eilers et al. 2019). Since MW dSphs have also a peculiar planar alignment (Pawlowski et al. 2014), Deason et al. (2021) opted to use halo stars, and after a thorough analysis of the possible recent accretions based on phase-space diagrams, they derive a total mass within 100 kpc of $6.07 \times 10^{11} M_\odot^3$, to which they associate systematics up to $1.2 \times 10^{11} M_\odot$. This is only marginally consistent with a very low MW mass and let promising a future

³ We do not discuss their extrapolation to $11.6 \times 10^{11} M_\odot$ for the MW total mass since it depends on the assumed NFW profile.

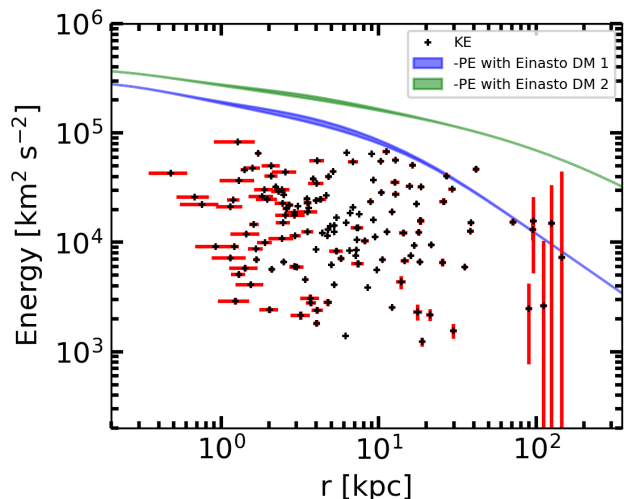


Fig. 6. Kinetic energy (KE) of the GCs from Vasiliev (2019) (crosses with red error bars) compared to the blue and green thick lines that indicate the potential energy (PE, absolute values) expected from the most likely and the heaviest Einasto model when associated to Model I for baryons, respectively. Error bars have been estimated with Monte Carlo randomly sampling by considering the errors in distance and radial velocity, as well as errors in proper motion and their covariance. The (small) thickness of the potential lines is due to the presence of the axisymmetric disk component.

study of Gaia EDR3 results combining both the MW RC and Globular Cluster motions (Wang et al. 2021, in preparation).

5. Summary

Rotation curves are major tools for determining the dynamical mass distribution in the Milky Way and spiral galaxies (Sofue 2013). They are also at the historical root for the need of DM in galactic haloes (Bosma 1978; Rubin et al. 1980), especially when they have been derived from the HI gas, which often extends much beyond the optical disk. Since that time, many estimates of the DM content in many spiral galaxies have been done generally through extrapolations of their observed rotation curves.

Here we have tested the most-used density profile to perform numerous analyses of galaxy RCs, namely the NFW density profile (Navarro et al. 1997), and its generalization to three parameters, the gNFW profile. We have considered the MW RC because it is one of the most accurately determined (Eilers et al. 2019), and also because the MW has not experienced a major merger since ~ 10 Gyr (Hammer et al. 2007; Helmi 2020). This supports the idea that its disk is dynamically virialized to at least 30 kpc, since Gnedin & Ostriker (1999) showed that it takes more than 3 dynamical times for a system to virialize after a perturbation.

Conversely to the NFW (or gNFW) profile for DM, the three-parameter Einasto profile (Einasto 1965, see also Retana-Montenegro et al. 2012) may account for many kinds of outer slopes, and provides a much better fit of the simulated DM properties (Dutton & Macciò 2014, and references therein), including for the physically motivated contracted halo (Cautun et al. 2020). It also shows consistent results able to fit the MW RC with most combinations of baryonic mass models, generating a plausible wide range of possible total masses (see Figures 2, 3 and 4).

Methodological problems due to the use of a too analytically constrained density model may affect the current estimates of the MW mass such as been done by Eilers et al. (2019). Perhaps

this also applies to the numerous galaxies for which the RC has been analyzed. Other galaxy RCs have yet to be analyzed using a three-parameter density model for the DM as it has been done in this paper. Such future investigations should focus first on galaxies having not experienced a recent major merger during which most of the disk has been resettled or rebuilt (Hammer et al. 2005, 2009; Hopkins et al. 2009). For example, such an event could complicate the interpretation of the M31 RC, whose recent, 2-3 Gyr ago major merger has had a much serious impact (see Hammer et al. 2018) than that of the Sagittarius passage near the MW. The later is suspected to have created vertical waves within the MW disk, although this is still disputed (see Bennett & Bovy 2020, and references therein), while the former has completely destroyed the M31 thin disk for stars with ages larger than 2 Gyr (see the modeling by Hammer et al. 2018 that reproduced the anomalous age-velocity dispersion discovered by Dorman et al. 2015). Besides this, it is also possible that other two-parameter models are affected in a similar manner, e.g., the isothermal model, rendering somewhat obsolete discussions about comparing the validity of such profiles for fitting RCs.

Using the Einasto profile, we find that the MW mass is mostly constrained by its slightly declining RC, which leads to higher χ^2 probabilities for small mass values (i.e., slightly below $3 \times 10^{11} M_\odot$) for the MW, though the less probable, higher values up to $18 \times 10^{11} M_\odot$ cannot be excluded. It leads to revise the available total mass range of the MW down to values that can be as small as $2.6 \times 10^{11} M_\odot$, and which are also consistent with the kinetic energy distribution of globular clusters. Further improvements on the MW RC accuracy will be invaluable for supporting or rejecting such small total masses. They would be invaluable in particular for determining precise orbits for the MW dSphs, for which, given the Gaia EDR3 precision, most uncertainties are now coming from our insufficient knowledge of the MW total mass.

Acknowledgements. We are very grateful for the useful and insightful discussions with Christina Eilers about the MW RC and the treatment of the systematics. We warmly thank Piercarlo Bonifacio for his careful advices and comments on the manuscript, and also Frederic Arenou and Carine Babusiaux for their contributions in the meetings during which the methodology of the paper has been adopted. We are acknowledging the support of the International Research Program Tianguan led by the French CNRS and the Chinese NAOC and Yunnan University.

References

- Allen, C. & Santillan, A. 1991, *Rev. Mexicana Astron. Astrofis.*, 22, 255
- Belokurov, V., Erkal, D., Evans, N. W., Koposov, S. E., & Deason, A. J. 2018, *MNRAS*, 478, 611
- Bennett, M. & Bovy, J. 2020, arXiv e-prints, arXiv:2010.04165
- Binney, J. & Tremaine, S. 2011, *Galactic dynamics* (Princeton university press)
- Bland-Hawthorn, J. & Gerhard, O. 2016, *ARA&A*, 54, 529
- Bosma, A. 1978, PhD thesis, Groningen University
- Bovy, J. & Rix, H.-W. 2013, *ApJ*, 779, 115
- Boylan-Kolchin, M., Bullock, J. S., Sohn, S. T., Besla, G., & van der Marel, R. P. 2013, *ApJ*, 768, 140
- Calchi Novati, S. & Mancini, L. 2011, *MNRAS*, 416, 1292
- Callingham, T. M., Cautun, M., Deason, A. J., et al. 2019, *MNRAS*, 484, 5453
- Cautun, M., Benítez-Llambay, A., Deason, A. J., et al. 2020, *MNRAS*, 494, 4291
- de Jong, J. T. A., Yanny, B., Rix, H.-W., et al. 2010, *ApJ*, 714, 663
- de Salas, P. F., Malhan, K., Freese, K., Hattori, K., & Valluri, M. 2019, *J. Cosmology Astropart. Phys.*, 2019, 037
- de Vaucouleurs, G. 1958, *ApJ*, 128, 465
- Deason, A. J., Erkal, D., Belokurov, V., et al. 2021, *MNRAS*, 501, 5964
- Dorman, C. E., Guhathakurta, P., Seth, A. C., et al. 2015, *ApJ*, 803, 24
- Dutton, A. A. & Macciò, A. V. 2014, *MNRAS*, 441, 3359
- Eilers, A.-C., Hogg, D. W., Rix, H.-W., & Ness, M. K. 2019, *ApJ*, 871, 120
- Einasto, J. 1965, *Trudy Astrofizicheskogo Instituta Alma-Ata*, 5, 87

- Fritz, T. K., Linden, S. T., Zivick, P., et al. 2017, *ApJ*, 840, 30
- Gao, L., Navarro, J. F., Cole, S., et al. 2008, *MNRAS*, 387, 536
- Gnedin, O. Y. & Ostriker, J. P. 1999, *ApJ*, 513, 626
- Grand, R. J. J., Deason, A. J., White, S. D. M., et al. 2019, *MNRAS*, 487, L72
- Hammer, F., Flores, H., Elbaz, D., et al. 2005, *A&A*, 430, 115
- Hammer, F., Flores, H., Puech, M., et al. 2009, *A&A*, 507, 1313
- Hammer, F., Puech, M., Chemin, L., Flores, H., & Lehnert, M. D. 2007, *ApJ*, 662, 322
- Hammer, F., Yang, Y., Arenou, F., et al. 2018, *ApJ*, 860, 76
- Hammer, F., Yang, Y., Arenou, F., et al. 2020, *ApJ*, 892, 3
- Haywood, M., Di Matteo, P., Lehnert, M. D., et al. 2018, *ApJ*, 863, 113
- Helmi, A. 2020, *ARA&A*, 58, 205
- Helmi, A., Babusiaux, C., Koppelman, H. H., et al. 2018, *Nature*, 563, 85
- Hinshaw, G., Larson, D., Komatsu, E., et al. 2013, *ApJS*, 208, 19
- Hogg, D. W., Eilers, A.-C., & Rix, H.-W. 2019, *AJ*, 158, 147
- Hopkins, P. F., Cox, T. J., Younger, J. D., & Hernquist, L. 2009, *ApJ*, 691, 1168
- Iocco, F., Pato, M., & Bertone, G. 2015, *Nature Physics*, 11, 245
- Jurić, M., Ivezić, Ž., Brooks, A., et al. 2008, *ApJ*, 673, 864
- Karukes, E. V., Benito, M., Iocco, F., Trotta, R., & Geringer-Sameth, A. 2020, *J. Cosmology Astropart. Phys.*, 2020, 033
- Klypin, A., Yepes, G., Gottlöber, S., Prada, F., & Heß, S. 2016, *MNRAS*, 457, 4340
- Mackereth, J. T., Bovy, J., Leung, H. W., et al. 2019, *MNRAS*, 489, 176
- Miyamoto, M. & Nagai, R. 1975, *PASJ*, 27, 533
- Mróz, P., Udalski, A., Skowron, D. M., et al. 2019, *ApJ*, 870, L10
- Navarro, J. F., Frenk, C. S., & White, S. D. M. 1997, *ApJ*, 490, 493
- Navarro, J. F., Hayashi, E., Power, C., et al. 2004, *MNRAS*, 349, 1039
- Navarro, J. F., Ludlow, A., Springel, V., et al. 2010, *MNRAS*, 402, 21
- Nesti, F. & Salucci, P. 2013, *J. Cosmology Astropart. Phys.*, 2013, 016
- Pawlowski, M. S., Famaey, B., Jerjen, H., et al. 2014, *MNRAS*, 442, 2362
- Pouliasis, E., Di Matteo, P., & Haywood, M. 2017, *A&A*, 598, A66
- Read, J. I. 2014, *Journal of Physics G Nuclear Physics*, 41, 063101
- Read, J. I., Iorio, G., Agertz, O., & Fraternali, F. 2016, *MNRAS*, 462, 3628
- Retana-Montenegro, E., van Hese, E., Gentile, G., Baes, M., & Frutos-Alfaro, F. 2012, *A&A*, 540, A70
- Rubin, V. C., Ford, W. K., J., & Thonnard, N. 1980, *ApJ*, 238, 471
- Sofue, Y. 2013, *PASJ*, 65, 118
- Sofue, Y. 2015, *PASJ*, 67, 75
- Stanek, K. Z., Udalski, A., Szymański, M., et al. 1997, *ApJ*, 477, 163
- Udrescu, S. M., Dutton, A. A., Macciò, A. V., & Buck, T. 2019, *MNRAS*, 482, 5259
- Vasiliev, E. 2019, *MNRAS*, 484, 2832
- Wegg, C., Gerhard, O., & Portail, M. 2016, *MNRAS*, 463, 557
- Zhao, H. 1996, *MNRAS*, 278, 488

Appendix A: Table A.1 with data of the MW RC and adopted error bars

The Table below provides the data on the MW RC given by Eilers et al. (2019), for which they have defined the statistical errors ($\sigma_{v_c}^-$ (km s⁻¹) and $\sigma_{v_c}^+$ (km s⁻¹)), and to which we have added the systematic error (see Sect. 2.1) in the last column as a fraction of the observed velocity, following the definition made in Eilers et al. (2019) Figure 4.

R(kpc)	v_c (km s ⁻¹)	$\sigma_{v_c}^-$ (km s ⁻¹)	$\sigma_{v_c}^+$ (km s ⁻¹)	$\Delta v_{\text{sys}}/v_c$
5.27	226.83	1.91	1.90	0.0045
5.74	230.80	1.43	1.35	0.0045
6.23	231.20	1.70	1.10	0.0045
6.73	229.88	1.44	1.32	0.002
7.22	229.61	1.37	1.11	0.0045
7.82	229.91	0.92	0.88	0.013
8.19	228.86	0.80	0.67	0.010
8.78	226.50	1.07	0.95	0.008
9.27	226.20	0.72	0.62	0.0088
9.76	225.94	0.42	0.52	0.0088
10.26	225.68	0.44	0.40	0.010
10.75	224.73	0.38	0.41	0.010
11.25	224.02	0.33	0.54	0.013
11.75	223.86	0.40	0.39	0.001
12.25	222.23	0.51	0.37	0.001
12.74	220.77	0.54	0.46	0.0046
13.23	220.92	0.57	0.40	0.0054
13.74	217.47	0.64	0.51	0.0054
14.24	217.31	0.77	0.66	0.010
14.74	217.60	0.65	0.68	0.0072
15.22	217.07	1.06	0.80	0.020
15.74	217.38	0.84	1.07	0.0257
16.24	216.14	1.20	1.48	0.0123
16.74	212.52	1.39	1.43	0.001
17.25	216.41	1.44	1.85	0.0182
17.75	213.70	2.22	1.65	0.0434
18.24	207.89	1.76	1.88	0.0377
18.74	209.60	2.31	2.77	0.0247
19.22	206.45	2.54	2.36	0.032
19.71	201.91	2.99	2.26	0.0385
20.27	199.84	3.15	2.89	0.056
20.78	198.14	3.33	3.37	0.041
21.24	195.30	5.99	6.50	0.010
21.80	213.67	15.38	12.18	0.086
22.14	176.97	28.58	18.57	0.13
22.73	193.11	27.64	19.05	0.13
23.66	176.63	18.67	16.74	0.13
24.82	198.42	6.50	6.12	0.045